Supplementary Material for Reconfigurable Exceptional Point-based Sensing with 0.001λ Sensitivity Using Spoof Localized Surface Plasmons

Yaoran Zhang,[a,†] Hao Hu,[a,‡] F. J. García-Vidal,[b] Jingjing Zhang,[c] Liangliang Liu,[a,*] Yu Luo,[a,d,*] and Zhuo Li[a,*]

[a]National Key Laboratory of Microwave Photonics, College of Electronic and Information Engineering, Nanjing University of Aeronautics and Astronautics, Nanjing, 211106, China
[b]Departamento de Física Teórica de la Materia Condensada and Condensed Matter Physics Center (IFIMAC), Universidad Autónoma de Madrid, E-28049 Madrid, Spain
[c]State Key Laboratory of Millimeter Waves, Southeast University, Nanjing 210096, China
[d]School of Electrical and Electronic Engineering, Nanyang Technological University, Nanyang Avenue 639798, Singapore

[†], [‡],These authors contribute equally to this work.
[*]Liangliang Liu, Email: llliu@nuaa.edu.cn; [*]Yu Luo, Email: yu.luo@nuaa.edu.cn; [*]Zhuo Li, Email: lizhuo@nuaa.edu.cn

This file includes:

Section S1 Phase distributions of the reconfigurable EPs

As shown in Figs. S1(a)-S1(e), the phase distributions in the plane 0.5 mm above the spoof plasmonic resonator exhibit the characteristics of vortex modes. Specifically, continuous phase changes of 6π, 8π, 10π, 12π, and 14π occur within one circular round of the ring resonator, which demonstrate the traveling wave properties at EP states. In contrast, when operating at DP states, a 180-degree phase discontinuity between each lobe is observed, sharply contrasting with the phase distributions of EP states. These distinctions in phase distributions provide additional evidence to support the characterization of DP states as standing wave modes and EP states as traveling wave modes.

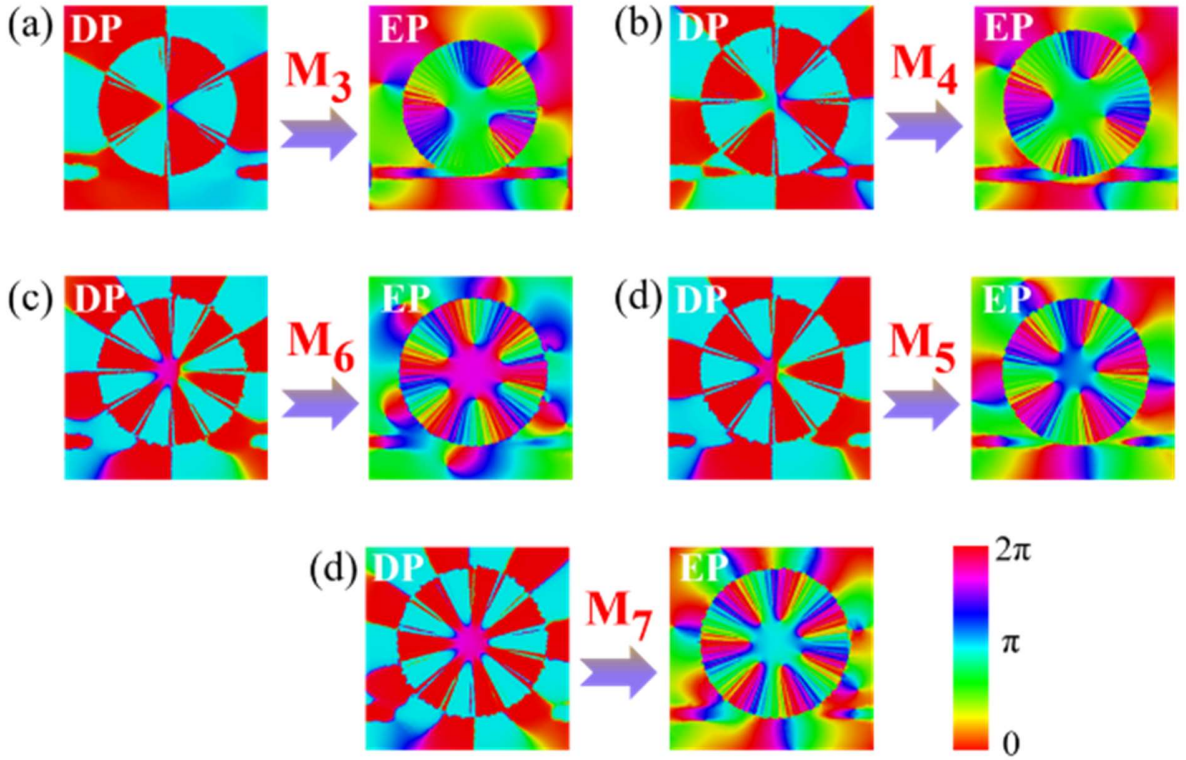

Fig. S1 Simulated phase distributions of the electric field E_z from standing wave (DP state) to traveling wave (EP state) of the reconfigurable EPs at (a) mode 3 (the sextupole mode), (b) mode 4 (the octupole mode), (c) mode 5 (the decapole mode), (d) mode 6 (the dodecapole mode) and (e) mode 7 (the fourteen-pole mode). The plots are in the plane 0.5 mm above the spoof plasmonic resonator.

Section S2 Fundamental theory of the EP-based sensor

Based on the two-mode approximation analysis of counter-propagating waves in the spoof LSPs resonator perturbed by a couple of Rayleigh scatterers, the total effective Hamiltonian in the travelling-wave system is given by the 2×2 matrix[22,24]

$$H_j^{(2)} = \begin{pmatrix} \omega_j^{(2)} & A_j^{(2)} \\ B_j^{(2)} & \omega_j^{(2)} \end{pmatrix}, \tag{S1}$$

with

$$\omega_j^{(2)} = \omega_j^{(0)} + \varepsilon_1 + \varepsilon_2 , \tag{S2}$$

$$A_j^{(2)} = \varepsilon_1 e^{-i2m_j\alpha_1} + \varepsilon_2 e^{-i2m_j\alpha_2} , \tag{S3}$$

$$B_j^{(2)} = \varepsilon_1 e^{i2m_j\alpha_1} + \varepsilon_2 e^{i2m_j\alpha_2} , \tag{S4}$$

where m_j represents the mode number of plasmonic mode j (with $j = 3, 4, 5, 6, 7$), $\omega_j^{(0)}$ denotes the frequency of the mode j without perturbation, α_1 (α_2) is the azimuthal angle of particle 1 (2) relative to the right periphery of the resonator, and ε_1 (ε_2) designates half of the frequency splitting induced solely by particle 1 (2). Note that the Hamiltonian $H_j^{(2)}$ mentioned above is non-Hermitian due to the complex nature of $\omega_j^{(0)}$ and ε_1 (ε_2), indicating the existence of losses.

The proposed exceptional-point sensor comprises of a spoof LSPs resonator and two deep-subwavelength metallic cylinders functioning as scatterers. Consequently, the Hamiltonian governing this sensor can be expressed as $H_{EP} = H_j^{(2)}$, where $A_j^{(2)}$ ($B_j^{(2)}$) represents the reflection of clockwise-propagating (counterclockwise-propagating) waves to counterclockwise-propagating (clockwise-propagating) waves. Achieving fully asymmetric backscattering is essential for attaining exceptional points. In the absence of perturbations, the diabolic point occurs

when $A_j^{(2)} = 0$ and $B_j^{(2)} = 0$, implying no backscattering between the counter-travelling waves. On the contrary, the exceptional point is described by $A_j^{(2)} = 0$ or $B_j^{(2)} = 0$, resulting in no backscattering into the CCW or CW waves while allowing backscattering into the opposite aspect.

The Hamiltonian of an exceptional-point sensor with a target scatterer is

$$H_j = H_{EP} + H_{DP}\,, \tag{S5}$$

where $H_j = H_j^{(3)}$, $H_{EP} = H_j^{(2)}$ and

$$H_{DP} = \begin{pmatrix} \varepsilon & \varepsilon e^{-i2m_j\alpha} \\ \varepsilon e^{i2m_j\alpha} & \varepsilon \end{pmatrix}. \tag{S6}$$

The perturbation strength of the target is $\varepsilon = \varepsilon_3$ and the relative azimuthal angle is $\alpha = \alpha_3$ in the matrix above. The frequency splitting here is described by[20]

$$\Delta\omega_{DP} = 2\varepsilon\,, \tag{S7}$$

$$\Delta\omega_{EP} = \Delta\omega_{DP}\sqrt{1 + \frac{A_j^{(2)}}{\varepsilon}e^{i2m_j\alpha}}\,. \tag{S8}$$

Additionally, when the perturbation strength $|\varepsilon|$ is sufficiently smaller than $\left|A_j^{(2)}\right|$, Eq. (S8) can be simplified to

$$\Delta\omega_{EP} = \Delta\omega_{DP}\sqrt{\frac{A_j^{(2)}}{\varepsilon}e^{i2m_j\alpha}} = 2\sqrt{A_j^{(2)}\varepsilon e^{im_j\alpha}}. \tag{S9}$$

As a consequence, the frequency splitting of EP sensors is proportional to $\varepsilon^{1/2}$, signifying an enhanced capability for detecting targets of sufficiently small sizes. Therefore, after the introduction of the target, the frequency splitting consequently results from the perturbation itself and the mutual contribution of the inherent backscattering and the perturbation. Note that this enhancement in sensitivity emanates from the intrinsic properties of exceptional points and

remains independent of the materials, system geometries, or characteristics of the scattering particles.

Section S3 Design of the suspended spoof plasmonic resonator

In order to efficiently excite the spoof plasmonic resonator, we suspend the spoof LSPs structure in an elevated position and place the microstrip line underneath the resonator. As depicted in Fig. S2(a), the dispersion curves of the periodic unit of spoof LSPs are all positioned to the right of the light line,[27, 28, 31, 32] indicating its non-radiative plasmonic mode nature. In comparison to structures directly printed on the substrate, the proposed suspended structure exhibits resonance modes that lie closer to the light line on the curve, signifying its lower field confinement and increased susceptibility to external scatterers. Figs. S2(b) and S2(c) illustrate the simulated electric field cross-sections of the proposed spoof LSPs and the printed resonator with the same intensity scaling at the operating plasmonic modes, respectively. Distinct comparisons reveal that the field of the traditional printed resonator localizes within the substrate. In contrast, the proposed suspended spoof LSPs exhibit prominent confined fields in the air below the resonator, exactly at the location where the particles are deposited.

Furthermore, the Q-factors of the sextu-, octu-, deca-, dodeca-, and fourteen-pole modes for the printed spoof LSPs are 178, 180, 185, 194, and 198, respectively. On the contrary, for the spoof plasmonic resonator we have developed, the Q-factors are significantly enhanced to 269, 460, 659, 814, and 676. These improvements demonstrate a considerable enhancement compared to traditional printed spoof LSPs. In conclusion, the spoof plasmonic resonator we have designed provides a novel platform for achieving tunable and reconfigurable EPs and paves the way for high performance sensors.

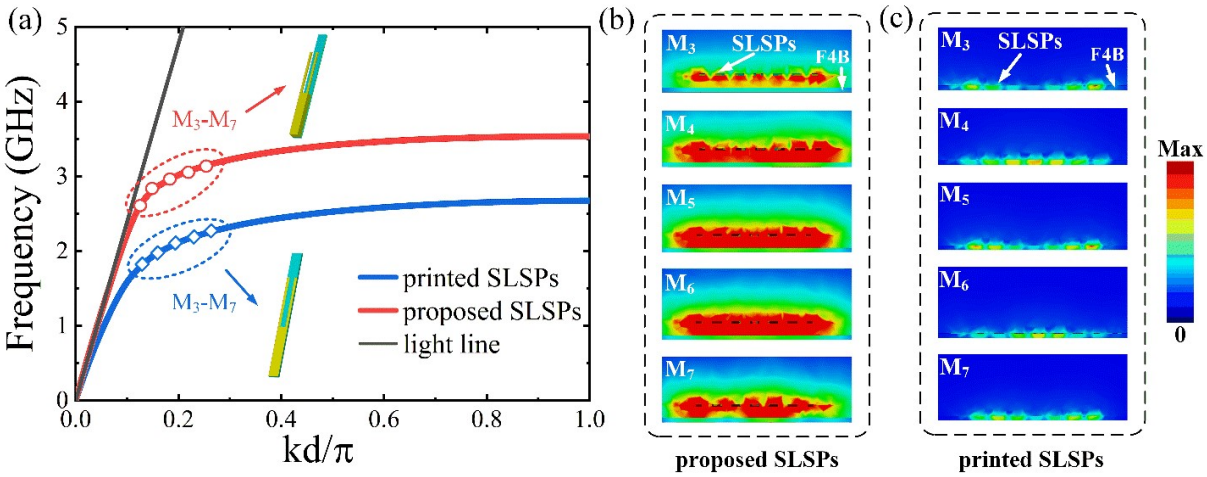

Fig. S2 (a) Dispersion curves of the spoof LSPs resonators. The red curve (proposed SLSPs) is closer to the light line than the blue curve (printed SLSPs) at the operating plasmonic modes, indicating weaker field confinements of the proposed spoof plasmonic resonator. The insets show schematic periodic units of the two types of SLSPs. Schematic illustrations depict the electric field $|E|$ cross-sections at the rim of (b) the proposed spoof LSPs and (c) the printed resonator with the same intensity scaling. The proposed suspended plasmonic resonator exhibits strong coupling with the scatterers below the structure, while the printed SLSPs only generate weak electric fields in the substrate.

Section S4 Details of the particles and measurement

To be specific, the targets detected by the reconfigurable EP sensors and the extra scatterers are metallic cylindrical particles, as depicted in Fig. S3. These particles vary in radius but share a consistent thickness of 2 mm, and they are fabricated from high-purity copper plates using precision laser cutting techniques. Additionally, the target cylinders are positioned below the left periphery of the spoof LSPs, tangent to the outer circumference of the ring resonator, i.e., $\alpha_3 = \pi$.

For the purpose of comparative validation, we have achieved reconfigurable EPs in the simulation for the sextu-, octu-, deca-, dodeca-, and fourteen-pole modes, respectively, as depicted in Fig. S4. The experimentally measured results agree well with the simulated outcomes. Additionally, single broadened resonance dips of the transmission coefficients and fully asymmetric reflection parameters validate the occurrence of EPs.

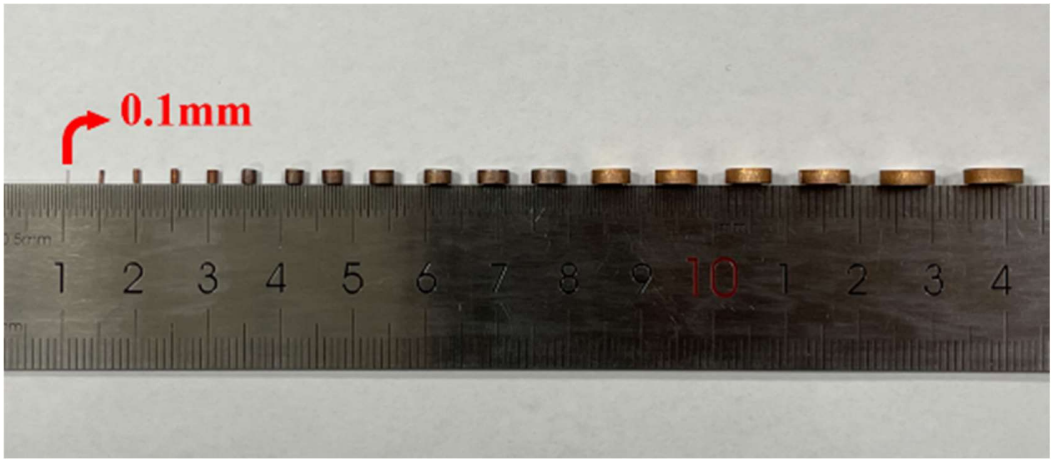

Fig. S3 Photograph of the targets detected by the sensors and the extra scatterers.

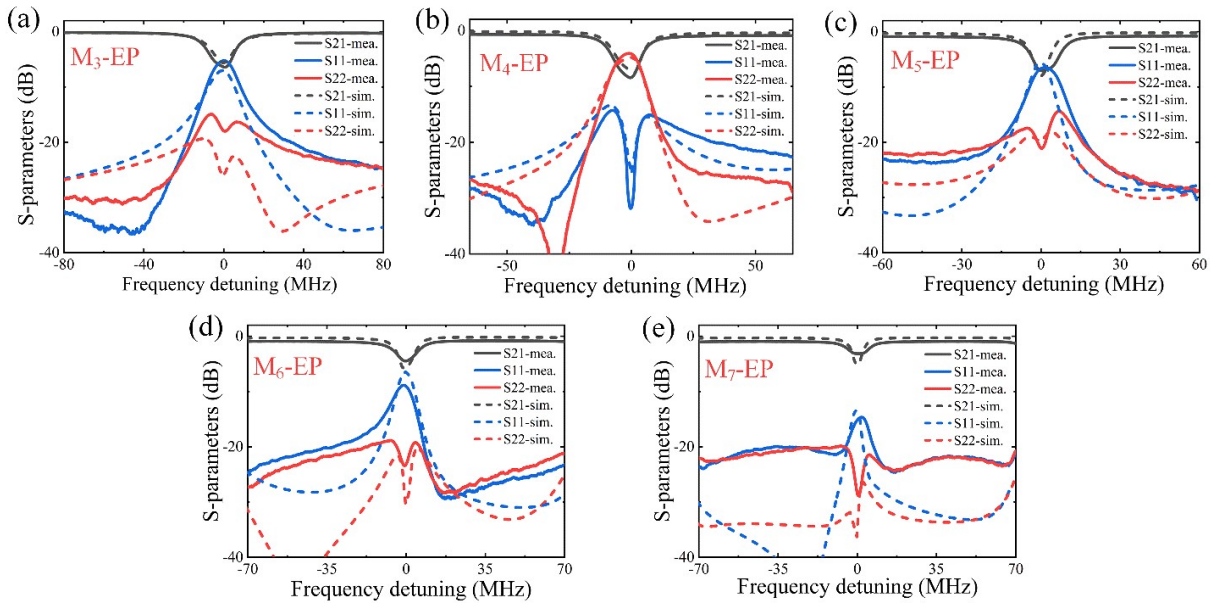

Fig. S4 Comparison of S-parameters of reconfigurable EPs between the simulated and measured results for (a) sextu-, (b) octu-, (c) deca-, (d) dodeca-, and (e) fourteen-pole modes.

Section S5 Measured spectra of the frequency responses

Furthermore, we selectively extract the detection results of the six smallest target sizes from the measured spectra of sensors operating at different modes, as depicted in Figs. S5 to S9. These figures provide clearer comparisons of the frequency splitting responses between DP and EP sensors when detecting small targets. The black vertical dashed lines highlight the enhancements of sensitivity in the EP sensors. It is essential to note that when the target size is sufficiently small, sensors operating at EP states possess resolution advantages over DP sensors. Specifically, EP sensors exhibit frequency splitting in the spectra, while DP sensors maintain single dips unchanged, indicating that EPs can enhance the detection capabilities. On the other hand, when the target is large enough to induce frequency splitting in both DP and EP sensors, the results obtained by EP sensors are significantly enhanced.

Detailed explanations of configuration of the sensor and the detection of targets with a diameter of 0.1 mm are presented in “Video 1_configuration of the DP sensor” and “Video 2_EP sensor at M7 and 0.001λ detection” in the supplementary files.

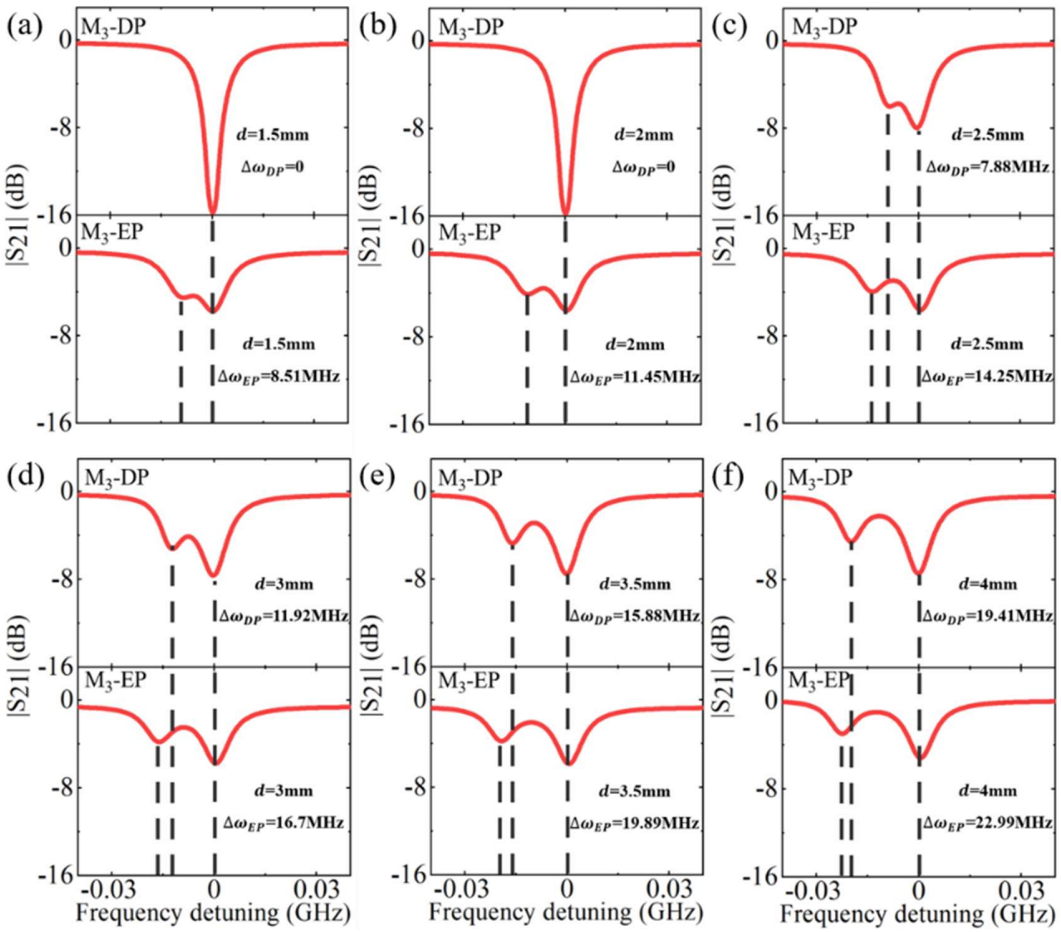

Fig. S5 Measured transmission spectra of DP and EP sensors at mode 3 (the sextupole mode) when detecting small targets.

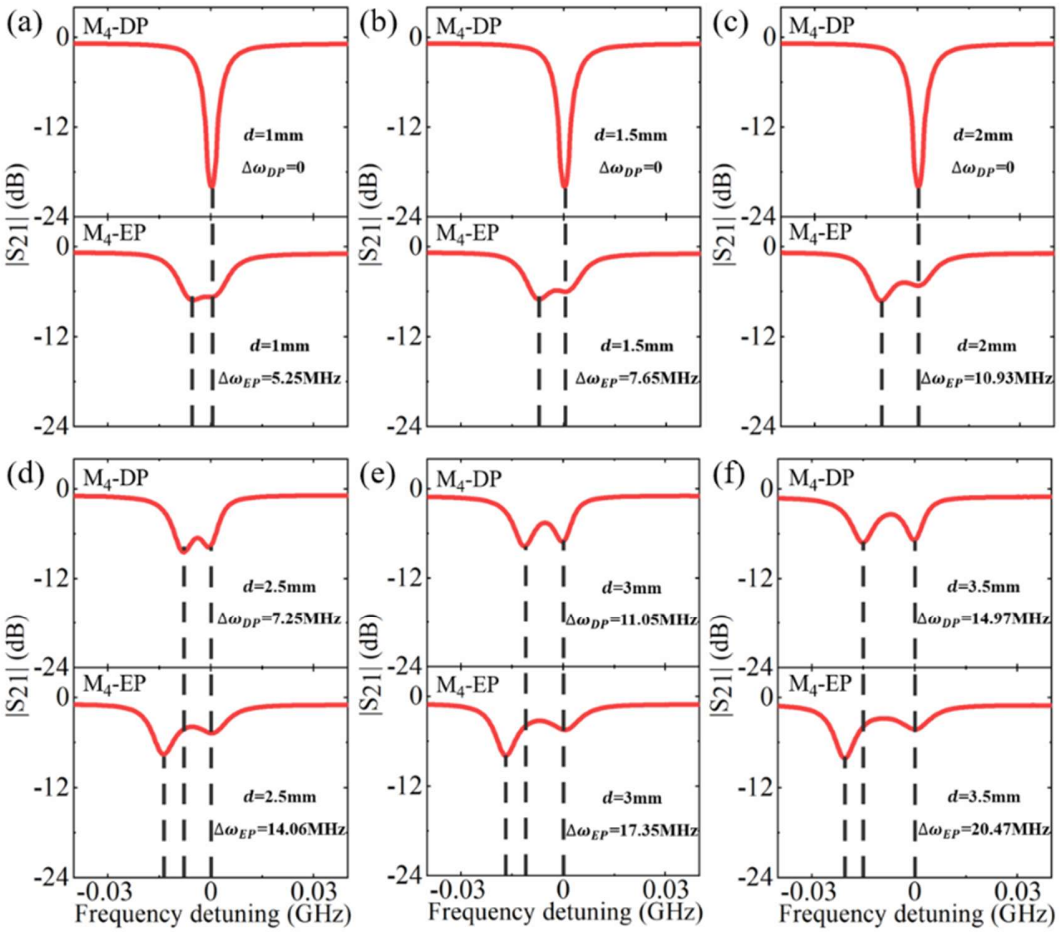

Fig. S6 Measured transmission spectra of DP and EP sensors at mode 4 (the octupole mode) when detecting small targets.

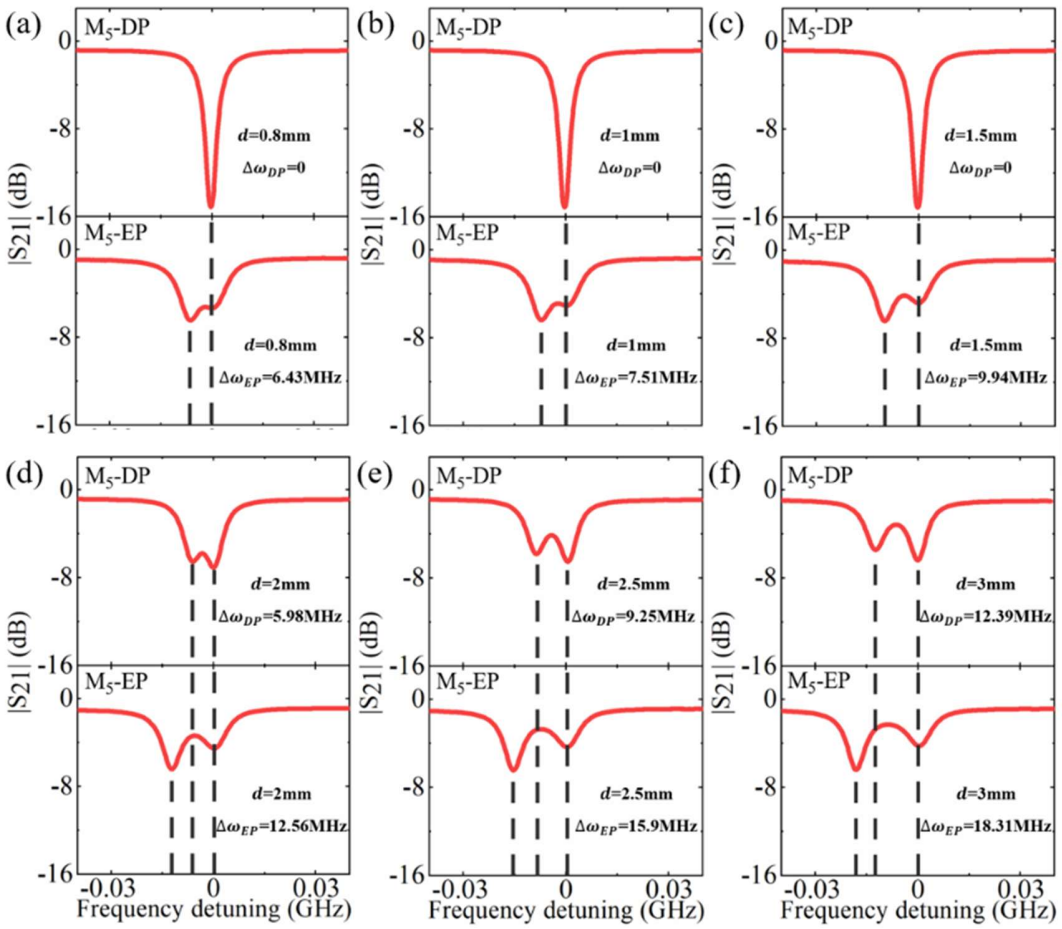

Fig. S7 Measured transmission spectra of DP and EP sensors at mode 5 (the decapole mode) when detecting small targets.

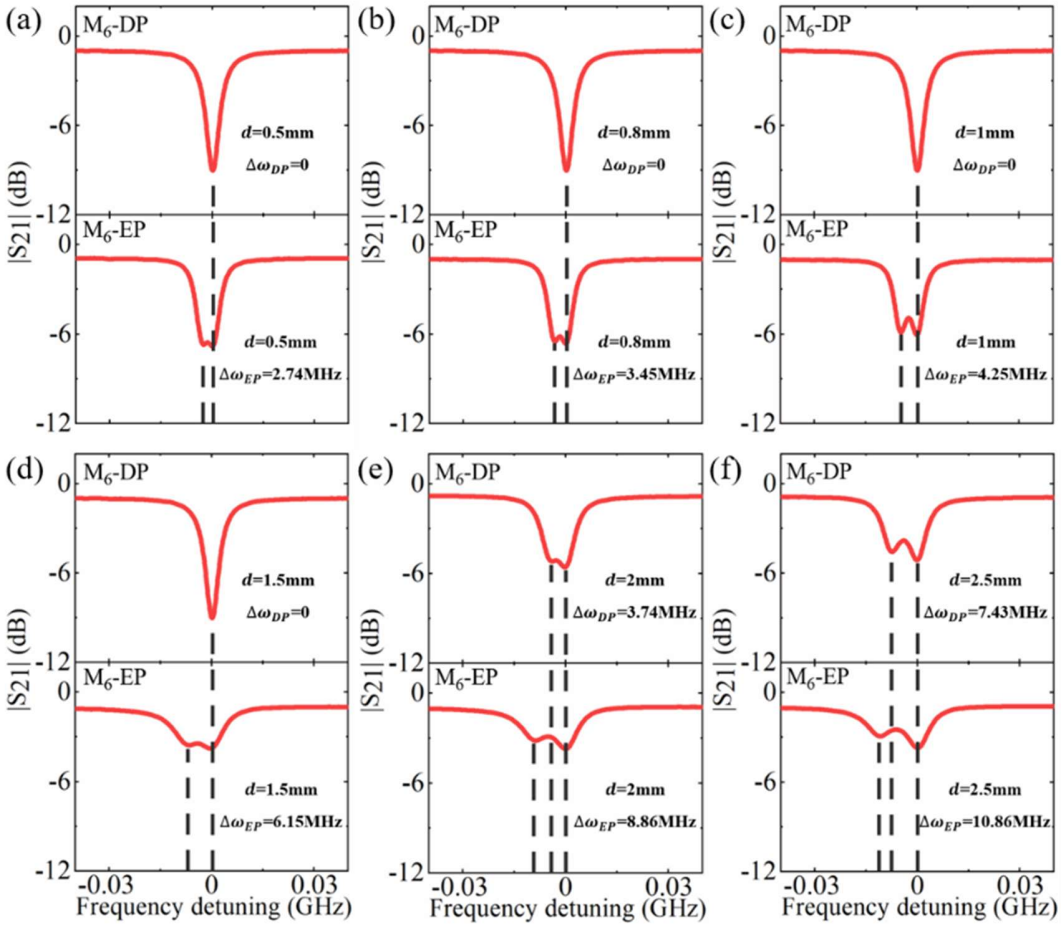

Fig S8 Measured transmission spectra of DP and EP sensors at mode 6 (the dodecapole mode) when detecting small targets.

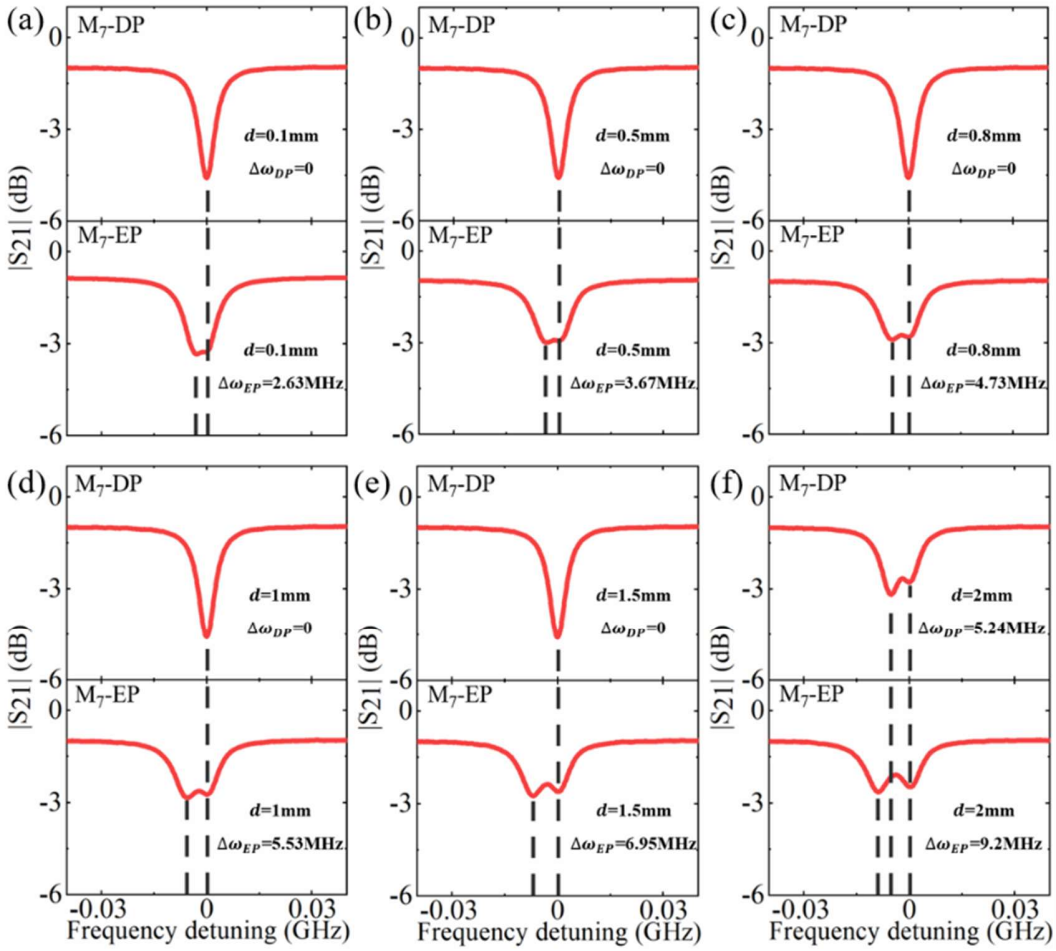

Fig. S9 Measured transmission spectra of DP and EP sensors at mode 7 (the fourteen-pole mode) when detecting small targets.

Section S6 Measured sensitivity enhancement of the reconfigurable EPs

The sensitivity enhancements of five tunable and reconfigurable EPs are listed in Table S1. We discuss the sensing capability of the proposed EP sensor by introducing targets with the diameters of around 0.02λ. All five EPs exhibit enhanced sensitivity and the frequency splitting of the DP and EP sensors experiences a gradual reduction from sextupole to dodecapole mode, while increasing slightly at the fourteen-pole mode.

Table S1 Comparison of measured sensitivity enhancement of the reconfigurable EPs

Mode	Diameter/mm	Electric length	$\Delta\omega_{DP}$/MHz	$\Delta\omega_{EP}$/MHz	Sensitivity enhancement
M_3@2.564GHz	2.5	0.021λ	7.88	14.25	1.8
M_4@2.765GHz	2.5	0.023λ	7.25	14.06	1.9
M_5@2.901GHz	2	0.019λ	5.98	12.56	2.1
M_6@3GHz	2	0.02λ	3.74	8.86	2.4
M_7@3.11GHz	2	0.02λ	5.24	9.2	1.8

Section S7 Reconfigurable EP sensor in the terahertz band

We conducted simulations to provide numerical evidence supporting our statement regarding the transferability of our proposed tunable and reconfigurable EP sensor to other frequency bands, such as terahertz frequencies. To be specific, we focus on investigating the sensitivity enhancement of the EP sensor operating at the sextupole mode (M_3) when detecting deep-subwavelength targets in the terahertz frequency range. We scale down the dimensions of the structure to 1/100 of the original sizes and utilize silver as the metal material due to its lower losses in the terahertz frequency range compared to copper. The microstrip line width of 28.2 μm overlaps with the resonator by $d_w = 20$ μm along the y-direction. The specific dimensions of the designed terahertz resonator are $R = 400$ μm (outer radius), $r = 200$ μm (inner radius), $a = 0.5d$ (periodicity), $t = 5$ μm (thickness), and $N = 60$ (number of grooves). The metal disk under the resonator has a radius of $R_d = r = 200$ μm and a thickness of $h_d = 25$ μm. Additionally, both the feeding line and the ground plane are 0.35 μm thick, while the F4B dielectric substrate has a thickness $h_s = 9.3$ μm, relative permittivity $\varepsilon_r = 2.2$, loss tangent $tan\delta = 0.003$, and side length $l_s = 1200$ μm.

First, we simulate the dispersion characteristics of the periodic structure of the suspended spoof LSPs, as shown in Fig. S10(a), with the cutoff frequency of around 0.36 THz. In the frequency range of 0.15-0.35 THz, the spoof plasmonic resonator also excites 9 resonance modes clearly, as illustrated in Fig. S10(b). It can be observed that due to the higher metal losses in the terahertz frequency range compared to the microwave frequency range, the insertion loss of the transmission coefficient is significant, approximately -1 dB. Then we fine-tune the system to the EP state using a pair of scatterers with diameters of 60 μm and 70 μm, with a relative azimuthal angle of 21.27 deg and the same thickness of 2 mm. Figure S10(c) shows the simulated transmission spectra of DP (top panels) and EP (bottom panels) sensors before (blue curves in left panels) and

after (red curves in right panels) introducing a target with a diameter of 25 μm (0.021λ at 0.253 THz) below the left periphery of the spoof LSPs, tangent to the outer circumference of the plasmonic resonator. The black vertical dashed lines in the right panels highlight the sensitivity enhancement by the factor of 1.7 (frequency splitting with 2.62 GHz in the DP sensor enhanced to 4.41 GHz in the EP sensor). The inset depicts fully asymmetric reflection coefficients, indicating the occurrence of EP. Furthermore, the schematic illustration of the terahertz reconfigurable DP and EP sensors is shown in Fig. S10(d). In addition, our simulations reveal the presence of standing waves in the DP state and traveling waves in the EP state, as evidenced by the amplitude and phase distributions of the electric field E_z.

Moreover, employing similar procedures and methodologies, we can design microwave reconfigurable EP sensors operating at other plasmonic modes (M_4-M_7) for the terahertz frequency range.

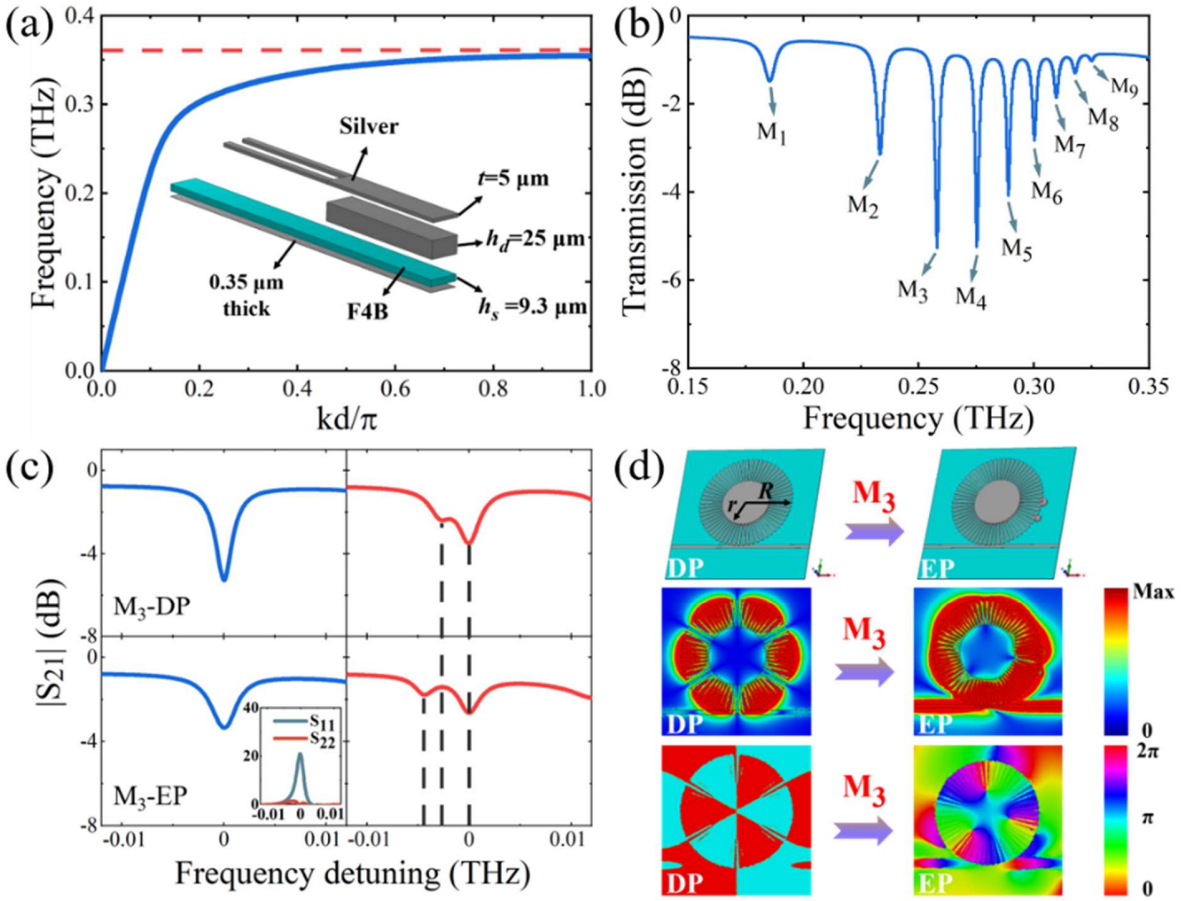

Fig. S10 (a) Simulated dispersion curves of the terahertz spoof plasmonic resonator. The inset shows the schematic periodic unit of the terahertz spoof LSPs. (b) Simulated transmission parameters of the terahertz DP sensor. (c) Simulated transmission spectra of DP (top panels) and EP (bottom panels) sensors at mode 3 (the sextupole mode) before (blue curves in left panels) and after (red curves in right panels) introducing a deep-subwavelength silver target. Black vertical dashed lines in right panels highlight the enhancements of sensitivity. The inset depicts fully asymmetric reflection coefficients, indicating the occurrence of EP. The abscissa axis of the inset figure represents frequency detuning (THz), while the ordinate axis represents the normalized reflection coefficients (a.u., arbitrary units). (d) Simulated amplitude and phase distributions of the electric field E_z from standing wave (DP state) to traveling wave (EP state) of the reconfigurable EP at mode 3 (the sextupole mode). The plots are in the plane 5 μm above the spoof plasmonic resonator.